Plasma Diagnostics with Tracer-Encapsulated Solid Pellet*)

Shigeru SUDO[1,2), Naoki TAMURA[1)], Sadatsugu MUTO[1,2)], Tetsuo OZAKI[1)],
Chihiro SUZUKI[1)], Hisamichi FUNABA[1,2)], Izumi MURAKAMI[1,2)], Daiji KATO[1,2)],
Shigeru INAGAKI[3)] and Katsumi IDA[1,2)]

[1)]*National Institute for Fusion Science, 322-6 Oroshi-cho, Toki 509-5292, Japan*
[2)]*The Graduate University for Advanced Studies, Hayama, Kanagawa 240-0193, Japan*
[3)]*Research Institute for Applied Mechanics, Kyushu University, 6-1 Kasuga-Koen, Kasuga 816-8580, Japan*

(Received 24 January 2014 / Accepted 11 March 2014)

The diagnostics method of a tracer-encapsulated solid pellet (TESPEL) has been developed. TESPEL consists of polystyrene as an outer shell and of specific material as a tracer in the core. Owing to the advantages of the TESPEL, the following results have been successfully obtained: (1) distinctive different feature of impurity transport between the plateau and Pfirsch-Schlüter regimes depending on the impurity source location which is analyzed with the STRAHL code, (2) specific feature of a non-local thermal transport such as abrupt increase of electron temperature in the plasma core in case of plasma cooling in the plasma periphery due to a small TESPEL injection, (3) spatially resolved energy distribution of the high energy particles obtained by a pellet charge exchange method, (4) longer impurity containment inside the magnetic island which is observed by depositing the tracers in the magnetic island by means of the TESPEL, and (5) identification of new spectral lines using interested atoms contained in the core of the TESPEL.

Keywords: TESPEL, pellet, tracer, impurity diagnostics, impurity transport

DOI: 10.1585/pfr.9.1402039

1. Introduction

The diagnostic method of a tracer-encapsulated solid pellet (TESPEL [1, 2]) has been developed, since the first TESPEL injection experiment was carried out at the Compact Helical System (CHS) for the purpose of the impurity transport study [3, 4]. After the TESPEL injection experiments at the Large Helical Device (LHD) started in 2000 [5, 6], the impurity transport study has been carried out [7–10], but it has been also found that the TESPEL method is available for the various diagnostic purposes. TESPEL consists of polystyrene (polymer in the form of $(C_8H_8)_n$) as an outer layer with the void of the typical diameter of 250 μm and of specific material as tracers in the core.

The advantages of the TESPEL method are summarized as follows:

(a) Direct local deposition of tracers inside the plasma is possible,
(b) Deposited amount of the tracer inside the plasma can be known precisely,
(c) Relatively wide selection of tracer materials is possible,
(d) Flexibility owing to a relatively wide range of pellet size enables the variable penetration depth of the tracer via the TESPEL.

Based on the above advantages of this method, the following various studies are being implemented:

(a) Impurity transport,
(b) Particle and thermal transport related to a magnetic island,
(c) Thermal transport with a non-local feature under a relatively low-collisionality condition,
(d) High energy particle observation with a pellet charge exchange (PCX) method, and
(e) Spectroscopy with interested atoms contained in the core of the TESPEL.

In the next section, the TESPEL injection system is briefly summarized, and the present research status of the above various fields is reviewed in the following sections.

Before starting the next sections, we would like to note one more advantage of the TESPEL, that is, the small disturbance on the bulk plasma. The TESPEL outer diameter ranges typically 500 ∼ 900 μm (for aiming at very shallow penetration, up to 400 μm is also used), and amount of the tracer particles is typically ∼ 10^{17} particles. This is less by a factor of 10^4 than that of the typical bulk plasma particles. On the other hand, the amount of C and H particles contained in the polystyrene pellet with a diameter of 720 μm is about 1×10^{19} particles for each. Thus, when these ions are fully stripped, the total electron number introduced by TESPEL causes the density increase of only 0.2×10^{19} m^{-3}, which is still smaller by a factor of more

author's e-mail: sudo@ms.nifs.ac.jp
*) This article is based on the invited talk at the 30th JSPF Annual Meeting (2013, Tokyo).

than 10 than the LHD plasma density in case of the usual impurity transport study. Thus, the disturbance on the bulk plasma by the TESPEL injection is relatively small. This is an attractive point. Furthermore, by containing multiple tracers in a TESPEL, the different tracer species can be compared simultaneously under the same plasma condition [11, 12].

2. Experiment Setup

The principle of the TESPEL diagnostics with the real photo of TESPEL is shown in Fig. 1 (a), and the schematic of TESPEL configuration is shown in Fig. 1 (b). The direct deposition of the tracers in the plasma with relatively small disturbance is an important feature of the TESPEL. The deposition location can be changed with adjusting the outer diameter and the shell thickness of TESPEL. To observe emission lines from tracers in the vacuum ultraviolet range, a high-resolution, time-resolving soft x-ray multichannel spectrometer (SOXMOS) [13] is used. To observe the characteristic x-ray lines such as the Kα line, the soft x-ray pulse height analyser (PHA) [14] is also equipped. The energy resolution is typically 160 eV, and a Be filter with a thickness of about 1 mm is inserted for avoiding low-energy photons. The TESPEL injection system [15] is shown in Fig. 2. The flange disk contains 60 ~ 90 TESPELs on the circumference. The tracer materials and their amount are registered for each position. This pellet holding disk and the counter disks having bearing are piled. Then, the disk is remotely rotated by a servomotor, and at a certain timing which is pre-scheduled, a TESPEL is ejected through a gun barrel by a He gas with a pressure of 20 ~ 30 atm. The typical TESPEL velocity ranges from 300 to 400 m/s. The TESPEL is guided by the guide tubes, and there is a fast gate valve between the guide tubes, thus, the system works well as a differential pumping system. In fact, when a TESPEL is ejected into the LHD chamber without plasma, the He pressure increase is not detectable.

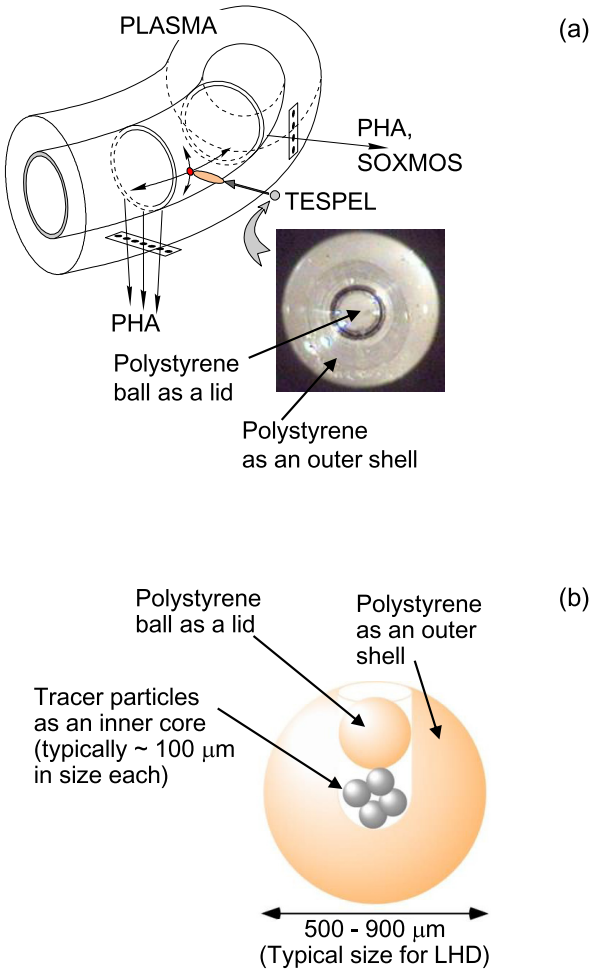

Fig. 1 (a) Principle of the TESPEL diagnostics with the real photo of TESPEL and (b) the schematic of TESPEL configuration.

3. Impurity Transport Study

3.1 Previous impurity transport studies

The impurity transport is one of key issues for developing a magnetically confined fusion reactor, because impurities could radiate substantial radiation power, which cools the bulk plasma. And, the existence of the impurities causes the dilution of the fuel. Considering the helium ash as impurity, it is a significant subject to find out how to evacuate the helium ash in an appropriate way.

So far, impurity behavior has been intensively studied in tokamaks and helical systems over the world for long years. For example, the impurity decay time versus the average electron density [16] is summarized for the helical systems: LHD, TJ-II, W7-AS in Fig. 3. General trend shows that the impurity decay time is increased, as the electron density is increased (up to a certain level). In the high-density region for the case of W7-AS, the impurity decay time becomes shorter as the electron density is increased in contrast to the general feature for the lower density case. This point is directly related with the present issue. We would like to show two more previous results. In Fig. 4, impurity decay time observation at W7-AS is shown with Al injection by a laser blow-off technique [17]. The high-density discharge (HDH) shows much shorter decay time compared to the case of the normal confinement (NC) discharge. Here, we would like to note that there are significant differences in determining the impurity source profile, which is quite important for the impurity transport study. In the laser blow-off experiment in W-AS, Al particles start to ionize in the scrape off layer, then penetrate into the plasma core with ionizing to higher charge states. In general, the impurity source (neutral Al^0) is unknown and the profiles of the low charge state ions are sensitive to the magnetic field configuration and plasma parameters at the edge. On the other hand, in the TESPEL, the initial impurity source profile is well determined by the ablation profile of the pellet. In Fig. 5, the impurity behavior ob-

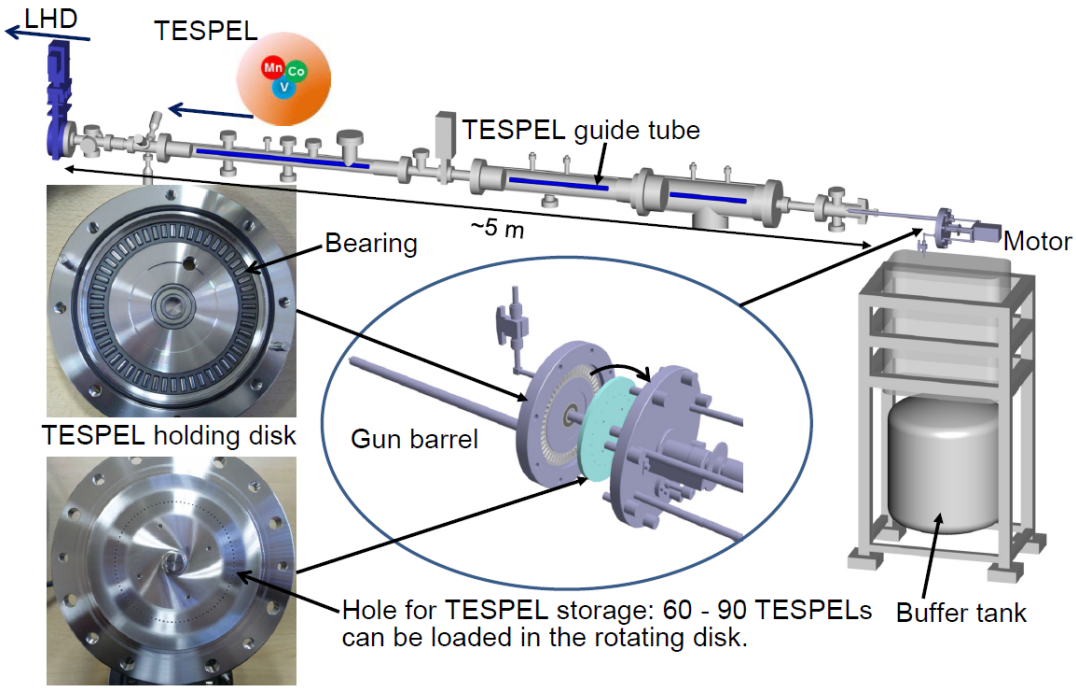

Fig. 2 TESPEL injection system.

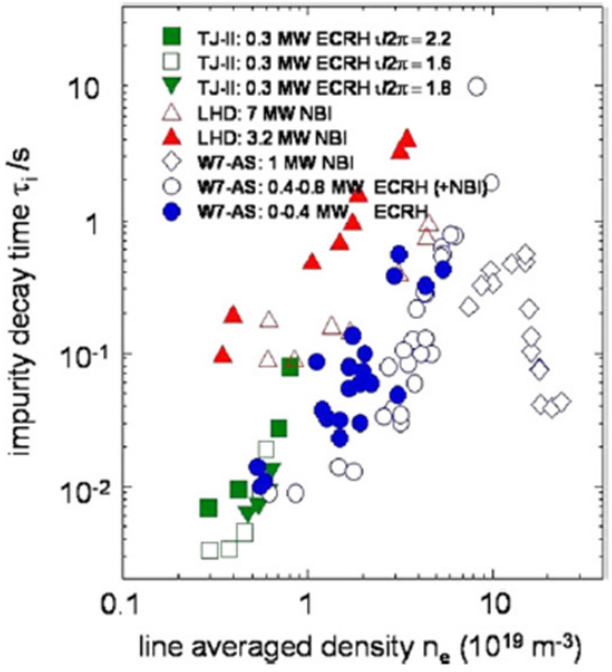

Fig. 3 Impurity decay time versus the average electron density for the helical systems: LHD, TJ-II, W7-AS, duplicated from Ref. [16].

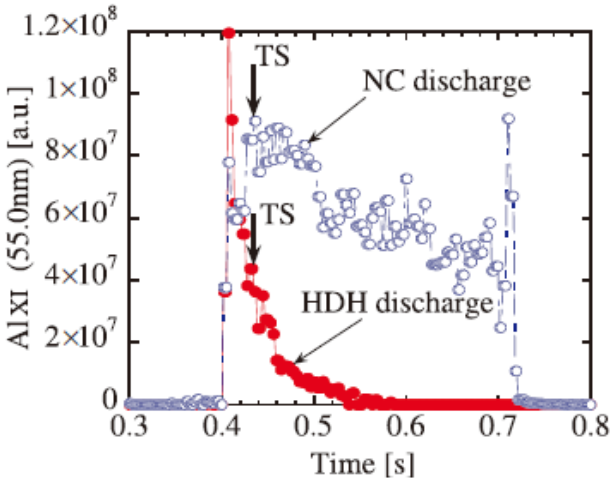

Fig. 4 Impurity decay time observation at W7-AS with Al injection by a laser blow-off technique, duplicated from Ref. [17]. The high-density discharge (HDH) shows much shorter decay time compared to the case of the normal confinement (NC) discharge.

served at LHD is shown on the $n_e(0)$–$T_e(0)$ diagram [18]. The solid circles indicate the plasmas with impurity accumulation and the open squares indicate the plasmas without accumulation. The open circles indicate the plasmas with the decrease of impurities or without impurity accumulation. It was concluded that the impurity is accumulated in the plateau regime, while it is not accumulated in the Pfirsch-Schlüter (PS) regime. Here it should be noted again that the relevant impurities are intrinsic ones, thus the impurity source is located outside of the plasma.

3.2 Present impurity transport studies

In contrast to the previous studies, we are using a TESPEL as shown in Fig. 1 for the purpose of the direct deposition of the tracers in the plasma. The elements of

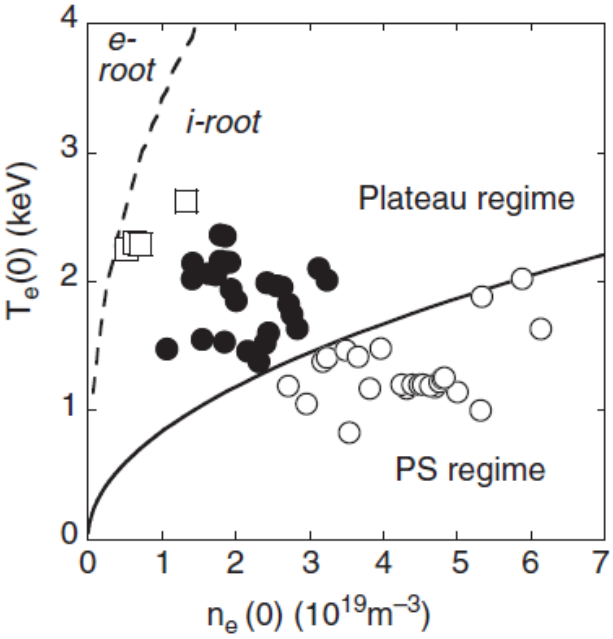

Fig. 5 Impurity behavior observed at LHD is shown on the $n_e(0)$–$T_e(0)$ diagram, duplicated from Ref. [18]. The solid circles indicate the plasmas with impurity accumulation and the open squares indicate the plasmas without accumulation. The open circles indicate the plasmas with the decrease of impurities or without impurity accumulation.

Table 1 Elements of tracers and intrinsic impurities.

Z	18	22	23	24	25	26	27	28
Atom	Ar	Ti	V	Cr	Mn	Fe	Co	Ni

The red color indicates tracer atoms and the purple color denotes intrinsic impurities from the wall. The green color corresponds to the atom via gas puffing.

tracers and intrinsic impurities are shown in Table 1. The intrinsic elements of Cr, Fe and Ni stem from the vacuum chamber made of stainless steel. Titanium (Ti) comes from the titanium gettering. So, it is natural to select V, Mn and Co as tracers in between those intrinsic elements. We could put simultaneously these triple tracers in the core of one polystyrene ball with a typical diameter of ~700 μm, and the tiny amount of those tracers is enough for observing the line emission from the tracers with a good S/N ratio as shown later. Ar is used as a simulator for the impurity existing outside of the plasma. The time integrated X-ray energy spectra of the Kα line emissions of V, Mn and Co and the intrinsic impurities for the plateau regime (LHD #106986) and PS regime (LHD #106999) are shown in Fig. 6. The average density n_e is 3.4×10^{19} m^{-3} for LHD #106986, and 6.6×10^{19} m^{-3} for LHD #106999. The NBI power is about 20 MW for the both cases. The density increase by TESPEL itself is relatively small compared to the bulk plasma. The Kα line intensities of the tracers in the

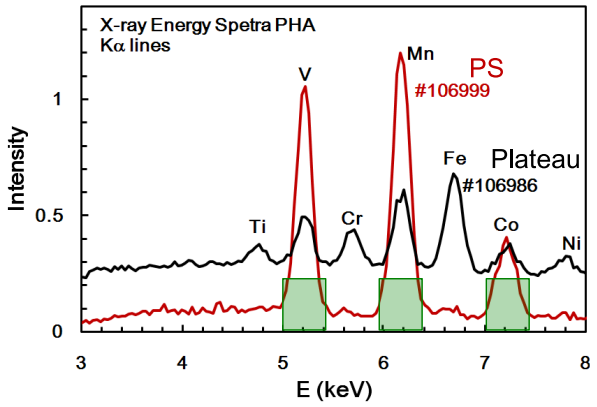

Fig. 6 X-ray energy spectra of the K_α line emissions of the tracers (V, Mn and Co) and the intrinsic impurities (Ti, Cr, Fe and Ni) for the plateau regime (LHD #106986, black line) and PS regime (LHD #106999, red line). Green boxes show the energy range corresponding to the Kα lines of the tracers.

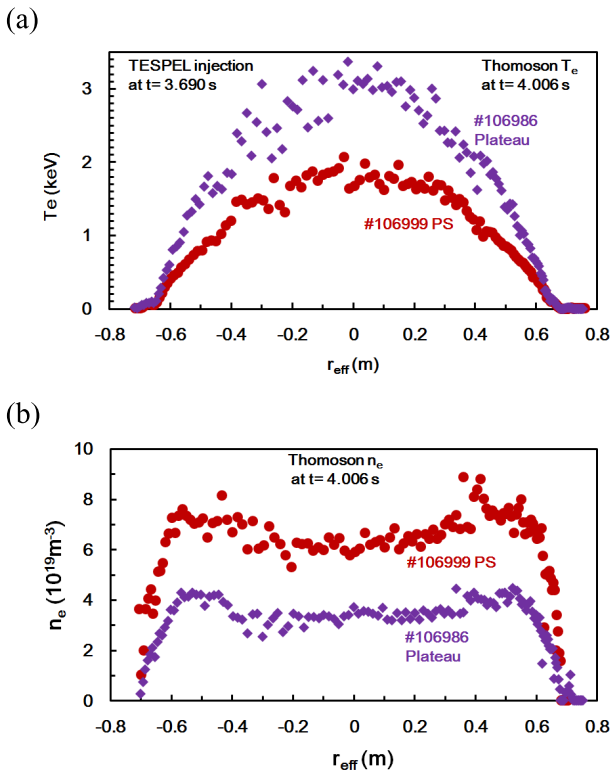

Fig. 7 Profiles of (a) electron temperature and (b) electron density for the plateau regime (LHD #106986, purple diamonds) and PS regime (LHD #106999, red circles).

PS regime are higher than those of the plateau regime. The Kα line emissions of the intrinsic impurities of Ti, Cr, Fe and Ni are clearly observed in case of the plateau regime. In contrast to this, these are completely suppressed in case of the PS regime. The temperature and density profiles at the timing of 312 ms after TESPEL injection are shown in Fig. 7. The central electron temperature $T_e(0)$ is 3 keV for LHD #106986, and 1.8 keV for LHD #106999.

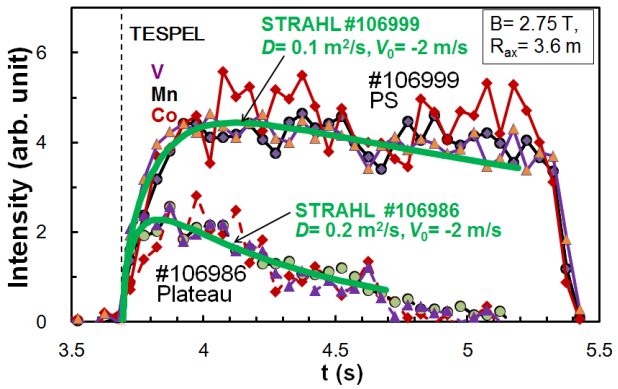

Fig. 8 Temporal evolutions of K_α intensities from the tracers (V, Mn and Co) in the two different collisional regimes. The STRAHL calculation with the assumed D (spatially flat) and V (inward pinch with the peak value of -2 m/s at $r_{\rm eff}/a_{99} = 0.9$) are also shown.

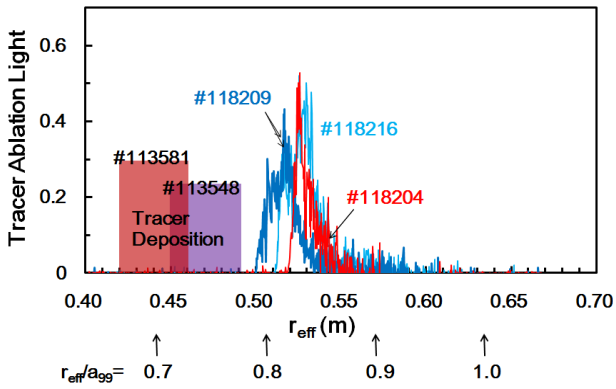

Fig. 9 Radial profile of the tracer ablation lights of the thin-shell-type TESPEL (LHD #118204: plateau regime, LHD #118209 and LHD #118216: PS regimes). The location of the tracer deposition by the solid-type TESPEL (LHD #113548: plateau regime and LHD #113581: PS regime) are also indicated for comparison.

Temporal evolutions of Kα intensities from the tracers (V, Mn and Co) in the two different collisional regimes are shown in Fig. 8. The STRAHL [19] calculation with the assumed particle diffusion coefficient D (spatially flat) and inward pinch V (with the peak value of -2 m/s at $r_{\rm eff}/a_{99} = 0.9$) are also shown, where $r_{\rm eff}$ is defined by a radius corresponding to the volume in a cylindrical approximation enclosed by each radial magnetic surface of the real plasma, and a_{99} is defined as the value of $r_{\rm eff}$ containing 99% of the whole plasma energy. The local emissivity is calculated by STRAHL. For comparing with the experimental data, the local emissivity is integrated along the line of sight. The experimental data is normalized at $t = \sim 3.9$ s. In the plateau regime, the decay feature of the calculated intensity with $D = 0.2\,{\rm m}^2/{\rm s}$ fits well with the experimental one as shown in the figure. In the PS regime, the experimentally obtained intensity is kept for a long time. For reference, the calculated one with $D = 0.1\,{\rm m}^2/{\rm s}$ is shown. Due to the slow decay feature, the sensitivity for fitting the diffusion coefficient is not enough in this case. So, the diffusion coefficient of $D = 0.1\,{\rm m}^2/{\rm s}$ should be considered as the upper limit. It should be also noted that the decay feature is essentially the same for the three different tracers. So, there is not a clear Z dependence on the decay time. The deposition location of the tracers are in the range of ρ ($\sim r_{\rm eff}/a_{99}$) = 0.6 ~ 0.75.

In order to investigate the case of the shallower location of the tracer deposition, we made a thin-shell-type TESPEL with smaller radius (600 μm) than the previous case (about 700 μm) and shell thickness of 75 μm. Tracer ablation light in the case of thin-shell-type of TESPEL (LHD #118204: plateau regime, LHD #118209 and LHD #118216: PS regimes) is shown in Fig. 9. The location of the ablation light for the thick-shell-type TESPEL (LHD #113548: plateau regime and LHD #113581: PS regime) is also shown for comparison. This "thick-shell-type" means

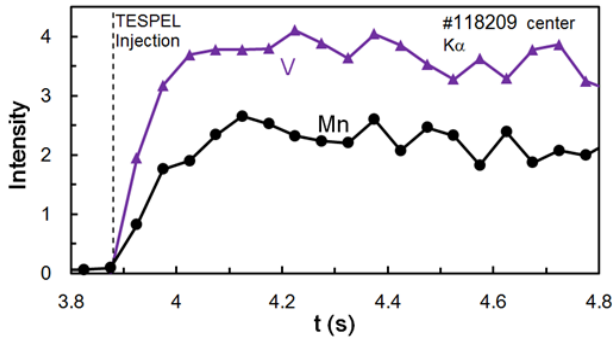

Fig. 10 Temporal evolutions of Kα intensities from the tracers (V and Mn) in case of the PS regime. In this case, the TESPEL is the thin-shell-type.

typically the thickness of the shell of 200-250 μm which is much larger than ~75 μm in case of thin-shell-type. As for the PS regime, the location of the deposition of the tracer particles is about ρ = ~0.7 in case of the thick-shell-type of TESPEL, while ρ = 0.8 ~ 0.85 in case of the thin-shell-type of TESPEL. Thus, the shallower deposition of the tracer particles is realized. Under this condition of the shallow deposition with using the thin-shell-type of TESPEL, the Kα line emissions from the tracers, V and Mn are shown in Fig. 10 in case of the PS regime. The Kα line intensities of these tracers are kept for a long time as the case of the tracer deposition location at ρ = ~0.7. So, essentially the long confinement feature of the impurity is applicable up to ρ = ~0.85 in the PS regime.

Next, it is interested to see how deep the impurities coming from the outside of the plasma penetrate into the plasma in case of the PS regime. In order to avoid the ambiguity of the impurity source amount, the Ar gas puffing is implemented as shown in Fig. 11. The amount of Ar

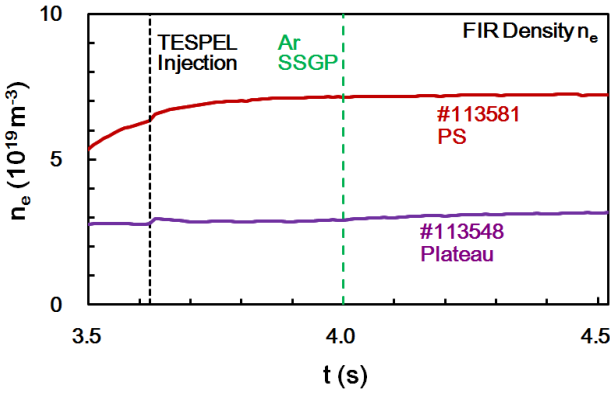

Fig. 11 Temporal evolutions of the electron density measured with the FIR interferometer for the two collisionality cases. Green dotted line indicates the timing of Ar SSGP (supersonic gas puffing).

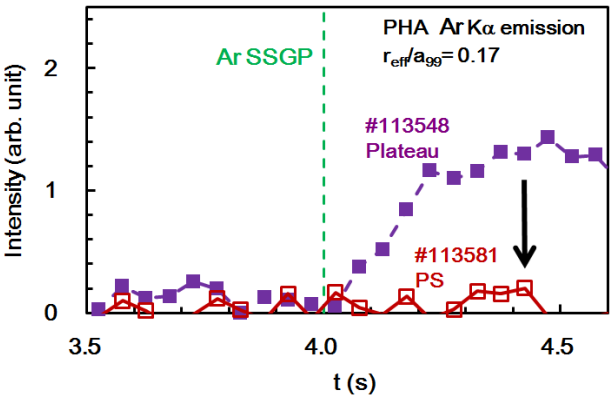

Fig. 12 Temporal evolutions of the Ar K_α intensity for the two collisionality cases.

particles is equivalent with that of the tracers. So, due to the very small number of the particles, the density rise due to the Ar gas puff is not detectable with the FIR system (The density increase at the timing of the TESPEL injection is due to the polystyrene, not due to the tracers.). Even with such a small amount, the intensity of the Ar Kα line is clearly detected, and the temporal evolution of the Ar Kα line intensity is shown in Fig. 12. The suppression of the Ar Kα line intensity in case of the PS regime indicates the shielding effect of the Ar particles. The suppression mechanism of the LHD plasma was studied by Kobayashi *et al.* [20, 21], and it will be briefly discussed later.

In contrast to the Ar Kα line emission, we observed the Be-like and Li-like line emissions from the Ar particles with enough S/N ratio even in case of the PS regime. In Fig. 13, the Ar Be-like line emissions (22.12 nm) for the plateau and PS regimes are shown. The Ar Li-like line emissions (35.39 nm) for the plateau and PS regimes are shown in Fig. 14. The intensity ratios of the PS versus plateau are shown with the black solid lines in Figs. 13 and 14. In order to see how deep the Ar particles penetrate

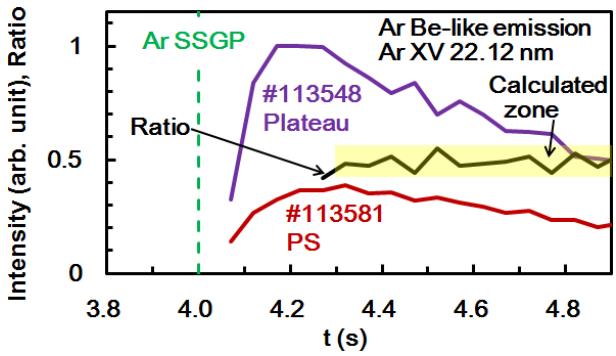

Fig. 13 Temporal evolutions of the Ar Be-like intensity for the two collisionality cases.

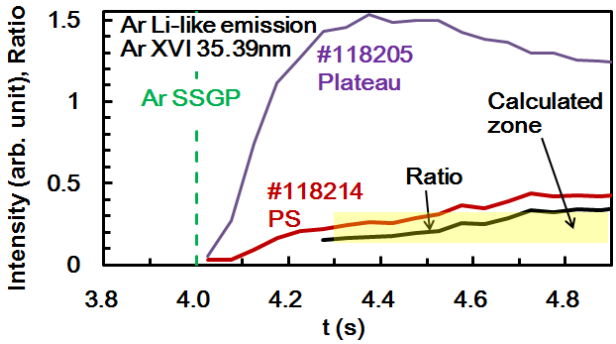

Fig. 14 Temporal evolutions of the Ar Li-like intensity for the two collisionality cases.

into the plasma in case of the PS regime, we used these intensity ratios shown as calculated zone with yellow color in the figures for both the Be-like and Li-like line emissions. At first, the temporal developments of the distribution of Ar Li-like ions calculated by the STRAHL code with neglecting the shield effect described above are shown in Figs. 15 (a) and (b) for both the collisionality regimes. The D and V values are used as the same ones as in Fig. 8. Then, it is seen that the Ar Li-like ions in case of the plateau regime are rather localized in the plasma periphery (at $\rho \sim 0.9$). On the other hand, the Ar Li-like ions in case of the PS regime are relatively widely distributed, and the total number of the Li-like ions is much more than the case of the plateau regime. But, this is contradictory to the experimental results. Thus, we count the integrated ion number from the plasma periphery to the certain radius of ρ ($\sim r_{\rm eff}/a_{99}$) in case of the PS regime. The integrated ion distribution ratio (ISDR) of the summation in the PS regime versus the plateau regime is shown in Fig. 16. The summation in the PS regime is taken from the plasma periphery to the radius of ρ. The summation in the plateau regime is taken for the whole radius. The total amount of gas-puffed Ar particles are the same for both the collisionality regimes. So, if we cut the existence of Ar particles inside of ρ in case of the PS regime, we should adjust the total Ar

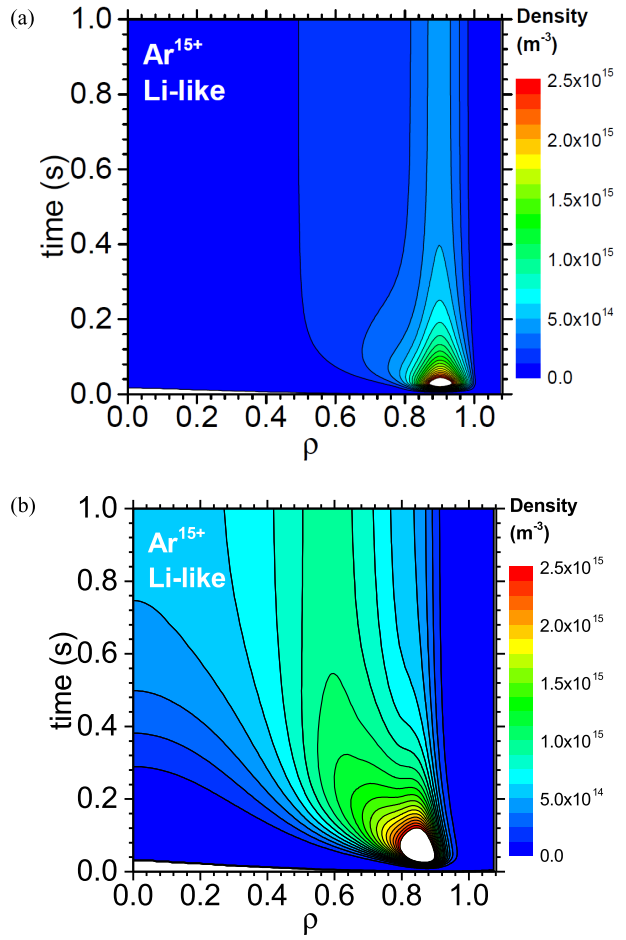

Fig. 15 Spatio-temporal developments of the Ar Li-like ion density calculated by the STRAHL code with neglecting the shield effect for (a) the plateau regime and (b) the PS regime.

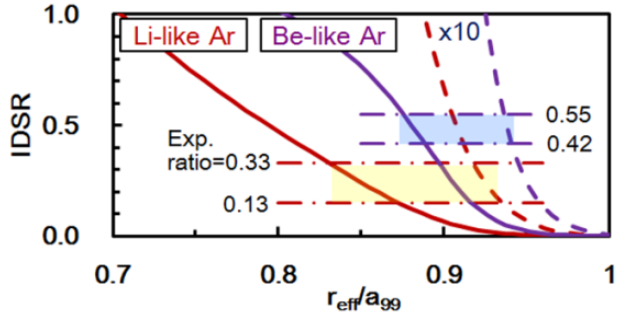

Fig. 16 Integrated ion distribution ratio (ISDR) of the summation in the PS regime versus the plateau regime. The summation in the PS regime is taken from the plasma periphery to the certain radius of ρ ($\sim r_{\rm eff}/a_{99}$). The summation in the plateau regime is taken for the whole radius.

particle number for calculation. The dotted line shows the case that the total Ar particle number is multiplied by a factor of 10. This factor is rather insensitive for the location. This is because the Ar Li- and Be-like ion fractions depend very strongly on the electron temperature in the plasma periphery. For example, in the PS regime, the Ar Li-like ion fraction is only 1×10^{-6} at $\rho = 1$ ($T_{\rm e} = 170$ eV), while 0.2 at $\rho = 0.95$ ($T_{\rm e} = 310$ eV) according to the NIST data [22]. So, the ratio is a very steep function of the electron temperature. The possible overlapping region for the Ar Li- and Be-like ion distributions consistent with the experimental results is $\rho = 0.88 \sim 0.93$. Considering the fact that the property of the tracers deposited within $\rho = 0.85$ is the same as in the case for the inner deposition of the tracers, it is concluded that the location of the discriminating the impurity property is around $\rho = 0.9$ (0.85 - 0.93) in case of the PS regime. So, the shielding mechanism is working in the plasma periphery [20, 21]. In the edge surface layers where the connection length is short, the friction force is working stronger in the higher density case. In the stochastic region, the thermal force is directed upstream due to the parallel temperature gradient, and the friction force is usually directed toward the divertor plates. The temperature gradient along the magnetic field line becomes smaller in the higher density case. This causes decrease of the thermal force. The ratio of the thermal and the friction forces depends strongly on the density, and the ratio is proportional to $n_{\rm e}^{-2.5\sim-3}$ [21]. So, in our experiments, the suppress of the influx of the impurities from the outside of the plasma may be due to the fact that the thermal force is decreased and the friction force dominates in case of the high density. From our experimental results, it is indicated that impurities coming from the outside of the plasma in the PS regime penetrate a little bit deeper ($\Delta\rho = \sim 0.1$) than the closed magnetic surface, but do not reach the long confinement region.

3.3 Impurity transport inside a magnetic island

In order to study the property of impurity transport inside the magnetic island, the titanium impurity was injected into the magnetic island O-point with the TESPEL [23, 24]. Here, the magnetic island O-point was expanded intentionally by using the auxiliary coil. The cross section including the TESPEL injection line and that of the 2-D tracer emission measurement with AXUVD (Absolute eXtreme UltraViolet photoDiode) arrays are shown in Figs. 17 (a) and (b), respectively. Reconstructed 2-D tracer emission images at (c) $t \sim 1$ ms and (d) $t \sim 8$ ms after the TESPEL injection are also shown in Fig. 17. For comparison, the magnetic island shape at the deposition location of the tracer impurity was changed from the O-point to the X-point. In the X-point case, the prolonged and localized emission as shown in Fig. 17 (d) was not observed. So far, the significant change of the neutral particle density has not been observed, when a phase of the magnetic island is changed. As the relevant magnetic island ($m/n = 1/1$) (at $\rho = 0.7 \sim 0.8$) exists well inside the plasma, the neutral

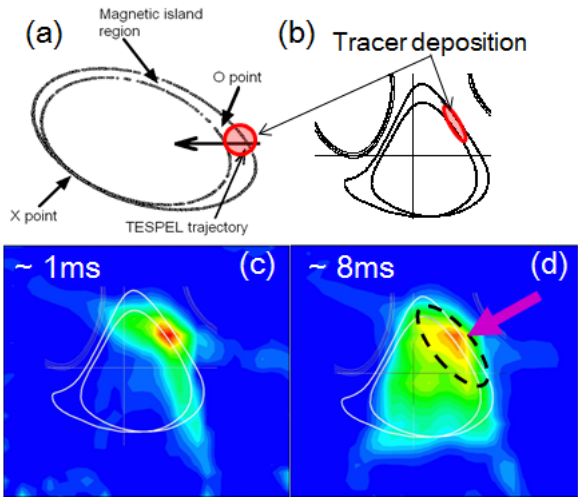

Fig. 17 (a) Tracer deposition inside the magnetic island can be achieved with a TESPEL method. (b) Corresponding cross section of 2-D tracer emission measurement with the AXUVD arrays. Reconstructed 2-D tracer emission images at (c) $t \sim 1$ ms and (d) $t \sim 8$ ms after the TESPEL injection.

density is much lower than that of the edge plasma. It is less possible that the neutral particle density plays a significant role in the difference of the transport of the tracers inside the magnetic island O-point or X-point. Thus, it seems that the impurities diffuse faster in the X-point case than the case of the O-point. In another words, this experiment shows apparently a long impurity confinement inside the magnetic island O-point. Also, a significant reduction of thermal transport is observed inside the magnetic island O-point [25, 26] by using the TESPEL. Concerning the study of heat and impurity inside the magnetic island O-point, the flexible property of the TESPEL is extensively utilized. That is, the outer diameter of TESPEL is selected so that appropriate penetration may be possible. This flexibility is also applied for the study of non-local feature of the electron thermal transport. It has been observed that the core electron temperature is abruptly increased just when the local electron temperature is decreased in the plasma periphery due to the TESPEL injection [27]. The phenomena occur in the relatively low-collisionality regime [28] (See also [29] for more detailed characteristics on non-local electron heat transport investigated by the TESPEL injection.). Although the formation of the electron internal transport barrier (e-ITB) can be seen in such a regime, the non-local core electron temperature rise in response to the edge perturbation is essentially different from the electron temperature rise by the improvement of the electron thermal transport due to the e-ITB formation [30]. Recently, the long-ranged low-frequency electron temperature fluctuation has been discovered in the plasma exhibiting the non-local core electron temperature rise [31], which would shed light on the physical mechanism of such a phenomenon. Such a local and small disturbance of electron temperature by the TESPEL injection is also applied for the study of the electron thermal transport in the vicinity of the electron internal transport barrier [32].

4. Fast Particle Observation

TESPEL has a possibility to measure energy spectrum of fast ions, which go away from the plasma after experiencing charge-exchange with a dense neutral cloud surrounding the TESPEL. As we know the location of the dense cloud by the spectroscopic measurement according to the TESPEL velocity measured and the TESPEL injection timing, so the temporal data measured by the local active fast neutral particle analyzer (NPA) can be converted to the spatial information. This method is called as a pellet charge exchange (PCX) method [33–41], and it has a good spatial resolution. One example is shown in Fig. 18 where the resonance layer is changed for the ICRF heating. The configurations of the standard resonance layer case: A and the central heating case: B for ICRF are shown in Fig. 18 (a). The Hα signal indicates the ablation of the polystyrene of TESPEL. The case A indicates more amount of fast particle production as shown in Fig. 18 (b) than the case B shown in Fig. 18 (c) [37]. The red circle shows the location of the energy increase in case A compared to case B.

For the quantitative analysis of the fast ion measurements, the density profile of the ablation cloud surrounding the TESPEL has been measured [42]. Figure 19 shows an example of the 2-D n_e profile in the TESPEL ablation cloud, which is deduced from the 2-D measurement of H_β (Stark broadening) profile in the cloud [43], which is obtained with a nine-optical-lens system with different narrow filters on a fast-shuttered C-MOS camera.

5. Application to the Spectroscopy

For the study of spectroscopy, interested atoms are put as tracer in TESPEL. It has been done especially in the range of EUV spectra from Nd, Gd [44, 45], Sn [46, 47] and W [48–50] and also the other heavy atoms. For example, spectra of highly charged Neodymium is studied with Neodymium tracer in the TESPEL having a diameter of 900 μm under the plasma condition with $T_e(0) = 2$ keV and $\bar{n}_e = 4\times10^{19}$ m^{-3}. In this case, a line due to $3d_{3/2}4p_{1/2}$–$3d_{3/2}4d_{3/2}$ transition (7.413 nm) of Ni-like Nd^{32+} has been assigned experimentally for the first time at LHD. The EUV emission of Sn around 13.5 nm will be applied for the future semiconductor lithography, and the emission of Gd around 6.8 nm is also interested for a shorter wavelength light source. These spectra are also investigated with the TESPEL method.

The EUV spectra of W particles injected by TESPEL are also observed, for example, in the wavelength regions of around 3 nm and 5 nm. Such data obtained at LHD will contribute to study of the edge plasma of ITER having a W wall.

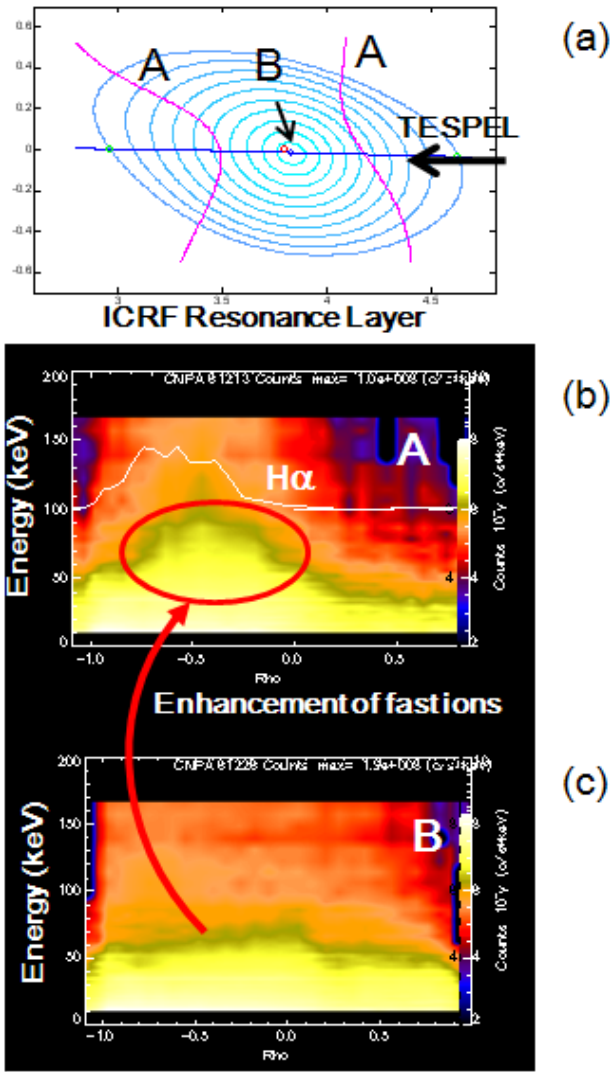

Fig. 18 (a) Location of the ICRF resonance layer for the standard heating case A and the central heating case B. Figures 18 (b, c) indicate that the fast particles are produced more in the case A than in the case B. The figures (b) and (c) are from Ref. [37], and red circle and arrow are added for highlighting the relevant point.

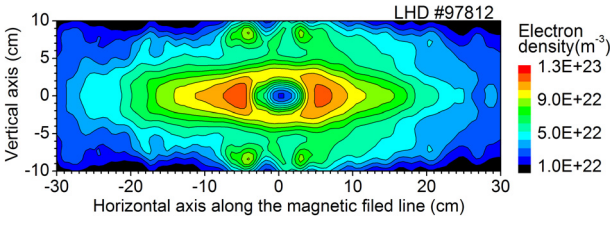

Fig. 19 2-D n_e profile in the TESPEL ablation cloud, which is deduced from the 2-D measurement of H_β profile in the cloud.

6. Discussion

The impurity behaviors in the plasma core and periphery have been studied by a triple-tracer TESPEL injection. So far it has been found that the impurity transport property in the plateau regime is different from that in the PS regime. The experimental data are analyzed with the STRAHL calculation. The property of the long confinement time of the impurity deposited inside the plasma in the PS regime suggests that impurities coming in a flake form may remain for a long time, and that the He ash produced inside the plasma may remain also for a long time in a future reactor machine. The high density operation is one of candidates for the helical type fusion reactor scheme. Especially, the extremely high density plasma called as a super dense core plasma has been successfully produced at LHD [51]. So, the collisionality in the plasma periphery of the future reactor relevant to the long confinement of impurities or He ash might be in the PS regime. As the impurity shielding effect or outflow of the impurity exists in the plasma periphery in the PS regime, if we can transport the impurity to the plasma periphery, the impurity may be flushed away. The concrete measure for this is the future subjects to be studied.

As for the impurity transport study, it is essential to measure the temporal developments of the location of the impurities. This is done here by comparing the specific emission line and the measured electron temperature profile with calculation (for example, STRAHL code). Several chords of such observation of the specific emission line will be helpful for spatial resolution. But, for the moment, the number of chords is very limited. We are now developing the measurement system of Kα lines in the chords with the order of 100 channels. On the other hand, there is a possibility to measure directly the spatially resolved impurities using a charge exchange recombination spectroscopy. This is based on the charge exchange of the impurity with the neutral beam of NBI for heating. There have been activities in the visible range [52,53] and soft X-ray range [54, 55] for this purpose. Although some signals were obtained through these activities, this method has not yet been used for a routine measurement due to the problem of the background light.

So far, 23 different elements have been utilized as tracer in TESPEL for the corresponding purposes as summarized in Table 2. For example, as a collaboration with the field of astrophysics, spectroscopic modelling for Fe ions in non-equilibrium ionization plasma has been developed taking advantage of the well measured electron temperature and density of the LHD plasma for the Fe emission data, and it is applied to analyze the solar spectra observed by HINODE [56]. Except for these tracers, TESPEL is also contributing to the investigation about the non-local transport owing to the flexibility of the pellet size, and it is also applied to the fast ion measurements. Thus, TESPEL are contributing to the various research fields.

As the outer layer of the TESPEL is polystyrene, the carbon particles are inevitably deposited in the plasma, and carbon line emissions are problem in some case. So,

Table 2 Implemented tracer atoms in TESPEL.

Purpose	Atoms for tracer	
Impurity transport	Li, F, Cl, Ti, V, Mn, Co, Ni	
Astrophysics	Fe	
W for fusion reactor	W	Nd, Sm, Gd, Tb, Dy, Er, Yb
EUV lithography	Sn	Ru, Gd, Tb
Biological microscopy	Mo, Au, Pb, Bi	

23 different atoms have been utilized. The third column of W for fusion reactor is for analyzing the W atom configuration with comparing the lower Z atoms. The third column of EUV lithography shows the shorter wavelength of the light source for higher accuracy than the standard atom of Sn. The atoms in the column of biological microscopy is for developing the light source for transparent to the water (in the range of 300 ~ 500 eV).

to avoid the carbon contamination, a tracer-encapsulated cryogenic pellet (TECPEL) is also developed [57–62]. In this case, the outer layer of the TECPEL is only hydrogen. The technology of producing and ejecting a TECPEL has been established [63]. The outer diameter of the TECPEL is about 3 mm, and it is not easy to change the diameter. This is the drawback of TECPEL compared to TESPEL.

7. Conclusion

It has been demonstrated that the advantages of TESPEL are useful for diagnostics in various fields. Especially, impurity transport study is carried out using the following unique features of TESPEL: (a) the local deposition of tracers inside the plasma is possible, (b) the deposited amount of the tracer inside the plasma can be known precisely, (c) a relatively wide selection of the tracer material is possible, and (d) the variable penetration depth is possible due to a relatively wide range of the size. As a result, it was found that the impurity transport characteristics between the plateau and Pfirsch-Schlüter regimes are quite different. Using TESPELs with different shell thickness and the Ar gas puffing, it is shown that the impurity source location is essential for the impurity transport feature. Namely, in the PS regime, the impurity deposited inside the plasma is kept for a long time, while the impurity coming from the outside of the plasma cannot enter into the plasma core. On the other hand, in the plateau regime, the impurity deposited inside the plasma flows away easily from the core of the plasma, and the impurity coming from the outside of the plasma enters relatively easily into the plasma core.

Except for the impurity transport study, TESPEL contributed to the following studies: (1) when the plasma periphery is cooled down by a small TESPEL injection, then abrupt increase of electron temperature in the plasma core is observed in case of relatively low collisionality regime. Such a non-local thermal transport has been studied intensively using TESPEL injection, (2) spatially resolved energy distribution of the high energy particles has been observed with a TESPEL pellet charge exchange method, (3) longer impurity containment inside the magnetic island is observed by depositing the tracers in the O-point of the magnetic island by means of the TESPEL injection, and (4) new spectral lines are identified using interested atoms contained in the core of the TESPEL.

Acknowledgments

S. Sudo thanks Professors B. Kuteev and V. Sergeev for long continuing collaboration on the TESPEL developments, and Prof. I. Viniar for the successful collaboration on the TECPEL developments. He would also like to acknowledge Drs. K.V. Khlopenkov, D. Kalinina, P.R. Goncharov, E. Veschev and Mr. I.A. Sharov for collaboration in the various fields related to the TESPEL activities. He thanks Prof. T. Norimatsu of Osaka univ., Dr. M. Takagi and Mr. N. Satoh of Hamamatsu Photonics K.K. for the support on the polystyrene pellet preparation which is essential for the TESPEL production. He would like to thank Mr. S. Goto and JECC TORISHA Co., Ltd. for the support of the TESPEL injector construction. He thanks Osaka Vacuum, Ltd. and Mr. M. Kanno for support on the design and construction of the pellet injection line with the differential pumping system. As for the TECPEL developments, the support from Mr. H. Ito and Nippon Sanso Corporation (the present Taiyo Nippon Sanso Corporation) is very much appreciated. The authors would like to thank the technical staffs of LHD for their excellent support on the experimental preparation. This work is supported by a Grant-in-Aid for Scientific Research (B) (No. 19340179 and 23360415) from JSPS Japan and budgetary Grants-in-Aid of ULHH012 and ULHH017 from NIFS.

[1] S. Sudo, J. Plasma Fusion Res. **69**, 1349 (1993).
[2] K.V. Khlopenkov and S. Sudo, Rev. Sci. Instrum. **69**, 3194 (1998).
[3] S. Sudo *et al.*, 17th IAEA CN-69 EXP1/18 (1998).
[4] K.V. Khlopenkov and S. Sudo, Plasma Phys. Control. Fusion **43**, 1547 (2001).
[5] N. Tamura *et al.*, J. Plasma Fusion Res. SERIES **4**, 442 (2001).
[6] S. Sudo *et al.*, Plasma Phys. Control. Fusion **44**, 129 (2002).
[7] N. Tamura *et al.*, J. Plasma Fusion Res. SERIES **5**, 400 (2002).
[8] S. Sudo *et al.*, Plasma Phys. Control. Fusion **45**, A425 (2003).
[9] N. Tamura *et al.*, Plasma Phys. Control. Fusion **45**, 27 (2003).
[10] S. Sudo *et al.*, J. Plasma Fusion Res. **2**, S1013 (2007).
[11] S. Sudo *et al.*, Nucl. Fusion **52**, 063012 (2012).
[12] S. Sudo *et al.*, Plasma Phys. Control. Fusion **55**, 095014 (2013).
[13] J.L. Schwob, A.W. Wouters, S. Suckewer and M. Finkenthal, Rev. Sci. Instrum. **58**, 1601 (1987).
[14] S. Muto *et al.*, Rev. Sci. Instrum. **72**, 1206 (2001).

[15] S. Sudo and N. Tamura, Rev. Sci. Instrum. **83**, 023503 (2012).
[16] R. Burhenn *et al.*, Nucl. Fusion **49**, 065005 (2009).
[17] K. Ida *et al.*, Plasma Phys. Control. Fusion **45**, 1931 (2003).
[18] Y. Nakamura *et al.*, Nucl. Fusion **43**, 219 (2003).
[19] K. Behringer, Rep. JET-R(87)08, JET Joint Undertaking, Abingdon (1987).
[20] M. Kobayashi *et al.*, Fusion Sci. Technol. **58**, 220 (2010).
[21] M. Kobayashi *et al.*, in Fusion Energy 2008 (Proc. 22nd Int. Conf. Geneva, 2008) (Vienna: IAEA) CD-ROM file EX/9-4 and http://www-naweb.iaea.org/napc/physics/FEC/FEC2008/html/index.htm.
[22] http://www-amdis.iaea.org/FLYCHK/
[23] N. Tamura *et al.*, J. Plasma Fusion Res. **78**, 837 (2002).
[24] N. Tamura *et al.*, J. Plasma Fusion Res. SERIES **8**, 0975 (2009).
[25] S. Inagaki *et al.*, Phys. Rev. Lett. **92**, 055002 (2004).
[26] K. Ida *et al.*, Nucl. Fusion **44**, 290 (2004).
[27] N. Tamura *et al.*, Phys. Plasmas **12**, 110705 (2005).
[28] N. Tamura *et al.*, Nucl. Fusion **47**, 449 (2007).
[29] N. Tamura *et al.*, Fusion Sci. Technol. **58**,122 (2010).
[30] N. Tamura *et al.*, Contrib. Plasma Phys. **50**, 514 (2010).
[31] S. Inagaki *et al.*, Phys. Rev. Lett. **107**, 115001 (2011).
[32] S. Inagaki *et al.*, Plasma Phys. Control. Fusion **46**, A71 (2004).
[33] P.R. Goncharov *et al.*, Rev. Sci. Instrum. **74**, 1869 (2003).
[34] P.R. Goncharov *et al.*, Rev. Sci. Instrum. **75**, 3613 (2004).
[35] T. Ozaki *et al.*, Rev. Sci. Instrum. **77**, 10E917 (2006).
[36] P.R. Goncharov *et al.*, Rev. Sci. Instrum. **77**, 10F119 (2006).
[37] T. Ozaki *et al.*, J. Plasma Fusion Res. **2**, S1072 (2007).
[38] T. Ozaki *et al.*, Fusion Eng. Des. **82**, 1251 (2007).
[39] T. Ozaki *et al.*, Rev. Sci. Instrum. **79**, 10E518 (2008).
[40] T. Ozaki *et al.*, J. Plasma Fusion Res. SERIES **8**, 1089 (2009).
[41] T. OZAKI *et al.*, Plasma Fusion Res. **7**, 2402138 (2012).
[42] N. Tamura *et al.*, Rev. Sci. Instrum. **79**, 10F541 (2008).
[43] I.A. Sharov *et al.*, in Proceedings of the 37th EPS Conference on Plasma Physics, Dublin, Ireland, 2010, p.5.131; also see http://ocs.ciemat.es/EPS2010PAP/pdf/P5.131.pdf.
[44] C. Suzuki *et al.*, J. Phys. B: At. Mol. Opt. Phys. **45**, 135002 (2012).
[45] C. Suzuki *et al.*, Phys. Scr. **T156**, 014078 (2013).
[46] C. Suzuki *et al.*, J. Phys.: Conf. Series **163**, 012019 (2009).
[47] C. Suzuki *et al.*, J. Phys. B: At. Mol. Opt. Phys. **43**, 074027 (2010).
[48] C.S. Harte *et al.*, J. Phys. B: At. Mol. Opt. Phys. **43**, 205004 (2010).
[49] C. Suzuki *et al.*, J. Phys. B: At. Mol. Opt. Phys. **44**, 175004 (2011).
[50] D. Kato *et al.*, Phys. Scr. **T156**, 014081 (2013).
[51] N. Ohyabu *et al.*, Phys. Rev. Lett. **97**, 055002 (2006).
[52] V.Yu. Sergeev *et al.*, Plasma Phys. Control. Fusion **44**, 277 (2002).
[53] D. Kalinina *et al.*, J. Plasma Fusion Res. **6**, 634 (2004).
[54] D. Kalinina *et al.*, J. Plasma Fusion Res. **80**, 545 (2004).
[55] D. Stutman *et al.*, Rev. Sci. Instrum. **76**, 013508 (2005).
[56] I. Murakami *et al.*, Plasma Fusion Res. **9**, 1401056 (2014).
[57] S. Sudo and H. Itoh, in Proceedings of the 16th SOFE conference, Illinois, 1995 (IEEE, New York) 2, 1589 (1996).
[58] S. Sudo, H. Itoh and K.V. Khlopenkov, Fusion Technol. **1**, 853 (1996).
[59] S. Sudo and H. Itoh, Fusion Eng. Des. **34-35**, 343 (1997).
[60] S. Sudo, H. Itoh and K. Khlopenkov, Rev. Sci. Instrum. **68**, 2717 (1997).
[61] I. Viniar *et al.*, Rev. Sci. Instrum. **72**, 2575 (2001).
[62] I. Viniar *et al.*, Fusion Eng. Des. **58-59**, 295 (2001).
[63] S. Sudo, I. Viniar, A. Lukin, P. Reznichenko and A. Umov, Rev. Sci. Instrum. **76**, 053507 (2005).